

CO_2 Dissolution Efficiency during Geological Carbon Sequestration (GCS) in Randomly Stratified formations

Yufei Wang^{1,2} Daniel Fernàndez-Garcia^{1,2} Maarten W. Saaltink^{1,2}

¹Dept. of Civil and Environmental Engineering, Universitat Politècnica de Catalunya, Jordi Girona 1-3, 08034 Barcelona,

Spain

²Associated Unit: Hydrogeology Group (UPC-CSIC)

Key Points:

- Mont Carlo simulations of Geological CO_2 Sequestration (GCS) in randomly stratified porous media;
- Dissolution trapping plays an important role in GCS, representing around 20% of the injected CO_2 ;
- The interplay between heterogeneity and buoyant forces controls the behavior of CO_2 migration and dissolution efficiency;
- In heterogeneity-controlled systems, permeability stratification enhances CO_2 dissolution efficiency by stretching the interface between gas and brine phases;
- The upscaling of permeability can lead to an underestimation of the dissolution efficiency.

Corresponding author: Yufei Wang, yufei.wang@upc.edu

Abstract

Geological Carbon Sequestration mitigates climate change by capturing and storing carbon emissions in deep geologic formations. Dissolution trapping is one mechanism by which CO_2 can be trapped in a deep formation. However, heterogeneity can significantly influence dissolution efficiency. This work addresses the injection of CO_2 in perfectly stratified saline formations under uncertainty. Monte Carlo two-phase flow compositional simulations involving the dissolution of CO_2 into brine and evaporation of water into the CO_2 -rich phase are presented. We systematically analyzed the interplay between heterogeneity and buoyant forces, which is shown to control the migration of the CO_2 plume as well as the temporal evolution of dissolution efficiency. Results show that when buoyant forces are important, vertical segregation controls the overall behavior of CO_2 , diminishing the influence of small-scale heterogeneity on dissolution. However, when buoyant forces are relatively small compared to the degree of heterogeneity, CO_2 migrates preferentially through high permeability layers and dissolution efficiency increases with heterogeneity due to the stretching of the CO_2 plume that enhances mixing. As a result, in this situation, the upscaling of permeability leads to an underestimation of the dissolution efficiency. A review of field sites shows that dissolution is heterogeneity-controlled in most real systems. Knowing that most numerical models cannot afford to represent heterogeneity at an adequate scale, results indicate that dissolution efficiency can be typically underestimated by a factor close to 1.5.

1 Introduction

Geological Carbon Sequestration (GCS), which reduces carbon emissions to the atmosphere by storing the captured CO_2 in deep geologic formations, is a promising technique to mitigate climate change [IPCC, 2005, 2008; Szulczewski *et al.*, 2012]. Four trapping mechanisms, taking place at different time-scales, are typically distinguished to confine the CO_2 in the subsurface [Kumar *et al.*, 2005; Riaz *et al.*, 2006; Bachu *et al.*, 2007; Vilarrasa *et al.*, 2010; Gasda *et al.*, 2012]. Structural trapping, which consists of sealing the $CO_2(g)$ with a low permeable caprock, is the most rapid but unstable mechanism because $CO_2(g)$ can potentially escape the formation through faults or failed wellbore casings during seismic activities. Mineral trapping, which considers that CO_2 can dissolve in brine and react with the rock-forming minerals, is the most stable but typically slow. At intermediate time-scales, the safety of GCS is attributed to capillary trapping (residual $CO_2(g)$) and dissolution trapping (dissolved aqueous $CO_2(aq)$ in brine). These two trapping mechanisms do not directly depend on the integrity of the formation [Van der Meer, 1995; Flett *et al.*, 2004; Nordbotten and Celia, 2006; Bryant *et al.*, 2008; Strandli and Benson, 2013]. Capillary trapping has been well studied in the literature [Juanes *et al.*, 2006; Ide *et al.*, 2007], but fewer studies address dissolution trapping even though a substantial amount of CO_2 can potentially dissolve in the formation due to the existence of large amounts of brine solvent [e.g., Flett *et al.*, 2004; Lee *et al.*, 2010]. Numerical results reported by Flett *et al.* [2004] have shown that dissolution can trap up to 33% of the injected CO_2 , which is quite close to the capillary trapping efficiency reported in the same field setting. Lee *et al.* [2010] have shown that dissolution trapping is more important than capillary trapping.

In homogeneous formations, the injected CO_2 is known to generate a smooth CO_2 plume, rising to the top of the formation by buoyant forces, and spreading laterally underneath the low permeability cap rock due to advection and dispersion; in the meanwhile, CO_2 dissolves into the brine over a long time [Lenormand *et al.*, 1988; Bryant *et al.*, 2008; Cottin *et al.*, 2010; Green and Ennis-King, 2010; Mouche *et al.*, 2010; Michael *et al.*, 2010; Bandara *et al.*, 2011; Oldenburg and Rinaldi, 2011; Strandli and Benson, 2013; Plampin *et al.*, 2014; Trevisan *et al.*, 2014; Mori *et al.*, 2015; Trevisan *et al.*, 2015]. However, natural formations are ubiquitously heterogeneous, affecting dissolution estimates in realistic settings. The literature in stochastic contaminant transport in saturated porous media has extensively demonstrated that heterogeneity can strongly deform solute plumes [e.g., Zinn and Harvey,

2003; Knudby and Carrera, 2005; Fernández-García et al., 2008; Dentz et al., 2011; Henri et al., 2015]. This deformation leads to the stretching and folding of the solute plume, which can increase the surface contact between the solute plume and the ambient groundwater. During the injection of CO_2 , similar effects are expected, potentially enhancing the capacity for CO_2 dissolution. Yet, results obtained in solute transport through saturated porous media cannot be directly extrapolated to CO_2 migration during geological carbon sequestration for two major reasons: the problem involves two fluid phases controlled by viscous and gravity forces with strong nonlinear constitutive equations, and the $CO_2(g)$ plume is affected by dissolution and evaporation.

The effect of permeability stratification during the injection of $CO_2(g)$ in GCS has been observed in several works, which have demonstrated that, after injection, a major proportion of CO_2 -rich phase can enter and move preferentially through relatively high permeability conduits or channels, creating erratic patterns [Stalkup and Crane, 1994; McGuire et al., 1995; Chadwick and Noy, 2010a,b; Oh et al., 2015; Rasmusson et al., 2015; Tsang et al., 2001; Obi and Blunt, 2006]. Data from Sleipner field site [Gregersen, 1998] in the North Sea, which is a reservoir formed by interbedded sandstones and mudstones, indicated that the injected $CO_2(g)$ was mostly present in several disconnected layers of relatively high permeability with a thickness of about 10 meters [Chadwick et al., 2004, 2005]. This illustrates that the stratification of permeability at the meter scale (in the vertical direction) can significantly affect the fate and transport of the $CO_2(g)$ plume. Little is known about the effect that these features have on CO_2 dissolution. Although a host of literature has assessed the fate and transport of the $CO_2(g)$ plume in GCS [e.g., Gunter et al., 2004; Humez et al., 2011; Kabera and Li, 2011; Oh et al., 2015], systematic high-resolution stochastic simulations of dissolution trapping in heterogeneous porous media remains lacking. The works of Ide et al. [2007], Hayek et al. [2009] and Oh et al. [2015] studied the effect of heterogeneity on capillary trapping, ignoring dissolution. Other authors [Doughty et al., 2001; Doughty and Pruess, 2004; Gershenzon et al., 2015a] have only analyzed dissolution trapping in a few idealized depositional settings. In numerical modeling studies, the small-scale variability of permeability is often not explicitly represented [Birkholzer et al., 2009; Hayek et al., 2009; Lee et al., 2010; Pruess and Nordbotten, 2011; Rasmusson et al., 2015; Onoja et al., 2019]. Qualitative or quantitative analysis of the impact of discounting the small-scale variability in modeling prediction estimates of geological carbon sequestration has not been reported.

In this paper, we present high-resolution two-phase flow numerical simulations of injected $CO_2(g)$ moving through a deep saline formation during geological carbon sequestration with the objective to: (i) study the effect of heterogeneity on CO_2 dissolution; and (ii) evaluate the impact of upscaling permeability on dissolution predictions. For this, we consider one of the simplest conceptual models of heterogeneity, that is, a perfectly stratified formation system in which the permeability varies only along the vertical direction. From a practical standpoint, we note that even though perfect stratification of permeability in natural field settings is seldom observed over large horizontal distances, this model can properly represent processes over relatively short distances compared to the horizontal integral scale of permeability, which can vary from few meters to thousands of meters [e.g., Schwartz, 2014]. Moreover, well-connected geological formations have been shown to behave similar to a perfectly stratified system, as both exhibit continuous paths of relatively high velocity [Zinn and Harvey, 2003]. This type of heterogeneity has been also used in a number of investigations that explore solute transport behavior in subsurface systems [Fernández-García et al., 2008; Mouche et al., 2010]. The numerical simulations we present consider a stochastic framework with multiple realizations of the permeability field, which are represented by a random space function and different degrees of heterogeneity. Dissolution efficiency is then characterized by the first two statistical moments to represent the mean behavior and its uncertainty. We show that heterogeneity and gravity forces control dissolution efficiency, and that for typical gravity forces, heterogeneity may substantially enhance dissolution efficiency. We also show that upscaling permeability can strongly compromise CO_2 dissolution predictions in highly heterogeneous systems.

The paper is organized as follows. We first present the problem and the mathematical description in Sections 2 and 3, respectively. We then introduce the computational approach adopted during simulations in Section 4. After this, in Section 5, we present the results. Section 5.1 shows how buoyant forces and heterogeneity affect CO_2 dissolution efficiency, and Section 5.2 illustrates how upscaling the permeability impacts on CO_2 dissolution efficiency. Finally, conclusions are summarized in Section 6.

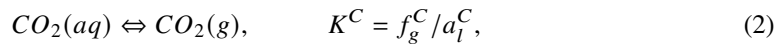
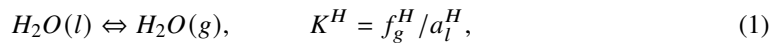
2 Problem Statement

We consider the injection of supercritical CO_2 through a fully-penetrating well in a deep confined saline formation. The formation is conceptualized as a perfectly stratified formation. Heterogeneity is represented by the spatial variability of the intrinsic permeability, which is assumed to vary in space only as a function of the z -coordinate. We consider the existence of two immiscible fluid phases, the brine phase (l) and the CO_2 -rich phase (g), which are separated by a distinct interface, characterized by a spatially varying retention curve. Brine is represented by a high-concentration solution of Sodium Chloride ($NaCl$) in water (H_2O). Initially, the formation is considered to be fully saturated with brine. Once injected, the CO_2 enters into the formation, displacing the brine and rising towards the top of the formation by buoyant forces. During the migration of CO_2 , dissolution of CO_2 into brine and evaporation of water into the CO_2 -rich phase takes place. The time scale for dissolution and evaporation is smaller than the time scale for transport, and therefore, we consider that reactions are always in local equilibrium [Xu *et al.*, 2004, 2011; Leal *et al.*, 2013]. Other reactions are not considered and the temperature is assumed constant. For brevity, the injected supercritical CO_2 is called gas.

3 Mathematical Description

3.1 Chemical System

The chemical system is composed of three chemical components $\{CO_2, H_2O, NaCl\}$. The first two chemical components $\{CO_2, H_2O\}$ can exist in both liquid and gas phases according to the equilibrium constants of dissolution and evaporation. Thus, mutual solubility between brine and CO_2 -rich phases is taken into account. $NaCl$ remains only in the brine phase. The changes in salinity due to dissolution/evaporation is assumed to be negligible and thereby the molality of $NaCl$ is assumed constant. In total, we have five chemical species: $CO_2(g)$, $CO_2(aq)$, $H_2O(g)$, $H_2O(l)$ and $NaCl(aq)$. The partition of the chemical species between phases is determined by the following equilibrium chemical reactions,



where the subscripts l , g and aq denote the liquid, the gas and the aqueous state, respectively, and the superscript C and H denote the CO_2 and H_2O components, respectively. K^H and K^C are the equilibrium constants, and f_g^β and a_l^β respectively denote the fugacity and the activity of the β chemical component. We follow the partitioning model for CO_2 -brine mixtures presented by *Spycher and Pruess* [2005] to estimate mass compositions in liquid and gas phases.

3.2 Mass Balance equations

The migration of CO_2 in the saline formation is simulated using a compositional approach. Given that the salinity is constant, we only need two mass balance equations. The

164 macroscopic mass balance equations for the two chemical components of interest $\{CO_2, H_2O\}$
 165 can be written as

$$0 = \mathcal{F}_1 = \sum_{\alpha=l,g} \left[\frac{\partial(\phi S_\alpha \rho_\alpha X_\alpha^H)}{\partial t} + \nabla \cdot (\rho_\alpha X_\alpha^H \mathbf{q}_\alpha) - \nabla \cdot (\phi S_\alpha \mathbf{D}_{\alpha\rho_\alpha} \nabla X_\alpha^H) \right] - Q_g^H, \quad (3)$$

$$0 = \mathcal{F}_2 = \sum_{\alpha=l,g} \left[\frac{\partial(\phi S_\alpha \rho_\alpha X_\alpha^C)}{\partial t} + \nabla \cdot (\rho_\alpha X_\alpha^C \mathbf{q}_\alpha) - \nabla \cdot (\phi S_\alpha \mathbf{D}_{\alpha\rho_\alpha} \nabla X_\alpha^C) \right] - Q_g^C, \quad (4)$$

166 where ϕ [-] is the formation porosity, S_α [-] is the saturation of the α -phase, ρ_α [$\text{kg}\cdot\text{m}^{-3}$] is
 167 the density of the α -phase, X_α^β [-] represents the mass fraction of component β in phase α , \mathbf{D}
 168 [$\text{m}^2\cdot\text{s}^{-1}$] is the hydrodynamic dispersion tensor, Q_g^H and Q_g^C [$\text{kg}\cdot\text{s}^{-1}$] are the source terms,
 169 and \mathbf{q}_α is the fluid flux associated with the α phase given by Darcy's law,

$$\mathbf{q}_\alpha = -\frac{\kappa \kappa_{r\alpha}}{\mu_\alpha} (\nabla p_\alpha + \rho_\alpha g \nabla z), \quad (5)$$

170 where κ [m^2] is the intrinsic permeability, $\kappa_{r\alpha}$ [-] is the relative permeability of phase α ,
 171 μ_α [$\text{Pa}\cdot\text{s}$] is the viscosity, p_α [Pa] is the fluid pressure, and g [$\text{m}\cdot\text{s}^{-2}$] is the gravitational
 172 acceleration. Mass balance equations are subject to the following constraints,

$$\omega X_l^H + X_l^C = 1, \quad (6)$$

$$X_g^H + X_g^C = 1, \quad (7)$$

$$S_l + S_g = 1, \quad (8)$$

175 where $\omega = 1 + 0.05844m_l^S$. Here, we have assumed that the salt only comprises *NaCl*, and
 176 the molality of *NaCl* (m_l^S) is fixed.

177 3.3 Constitutive Equations

178 The saturation of the liquid phase is assumed to be known from the capillary pressure
 179 through the $CO_2 - H_2O$ retention curve. In this work, we used the *van Genuchten* [1980]
 180 model for the retention curve, which determines that

$$S_{le}(p_c) = \begin{cases} 1, & p_c < 0 \\ [1 + (\sqrt{\frac{\kappa}{\kappa_g}} \alpha_p p_c)^{n_p}]^{-m_p}, & p_c \geq 0, \end{cases} \quad (9)$$

181 where p_c is the capillary pressure between the two immiscible fluids, defined as $p_c = p_g - p_l$,
 182 κ_g [m^2] is the geometric mean of the intrinsic permeability, $m_p = 1 - 1/n_p$, α_p [bar^{-1}] is the
 183 scaling parameter of the retention curve, and S_{le} is the effective liquid saturation, defined as

$$S_{le} = \begin{cases} 1, & S_l > 1 - S_{gr} \\ \frac{S_l - S_{lr}}{1 - S_{lr} - S_{gr}}, & S_{lr} \leq S_l \leq 1 - S_{gr} \\ 0, & S_l < S_{lr}, \end{cases} \quad (10)$$

184 where S_{lr} [-] and S_{gr} [-] are the residual saturations of brine and CO_2 -rich phases, respec-
 185 tively. The Leverett J -function has been used to describe the relationship between the entry

186 pressure and the permeability of the porous medium [Juanes *et al.*, 2006; Plug and Bruining,
 187 2007; Krevor *et al.*, 2011, 2015]. The porosity is assumed constant. The relative permeabili-
 188 ties for the two phases are respectively given as

$$\kappa_{rl} = \kappa_{rlm} \cdot (S_{le})^{\epsilon_p} [1 - (1 - S_{le}^{1/m_p})^{m_p}]^2, \quad (11)$$

$$\kappa_{rg} = \kappa_{rgm} \cdot (1 - S_{le})^{\gamma_p} (1 - S_{le}^{1/m_p})^{2m_p}, \quad (12)$$

189 where κ_{rlm} , κ_{rgm} , ϵ_p and γ_p are the scaling parameters. Hysteresis of the retention curve
 190 and the relative permeability curve is not considered. The dispersion tensor is given as

$$\mathbf{D}_\alpha = D_m \mathbf{I} + \alpha_L |\mathbf{v}_\alpha| + (\alpha_L - \alpha_T) \frac{\mathbf{v}_\alpha \mathbf{v}_\alpha^t}{|\mathbf{v}_\alpha|}, \quad (13)$$

191 where \mathbf{I} is identity matrix, D_m is molecular diffusion coefficient, α_L and α_T are respectively
 192 the longitudinal and transverse dispersivities, and $\mathbf{v}_\alpha = \mathbf{q}_\alpha / (\phi S_\alpha)$ [Saaltink *et al.*, 2013].
 193 The density and viscosity of the two fluids is affected by the fluid pressures and their mass
 194 compositions according to Garcia [2003] and Wang [2022].

195 3.4 Numerical Solution

196 We developed a MATLAB-based fully-coupled integrated finite difference code to
 197 solve the system of transport equations given by (3) and (4) using a fully implicit method
 198 based on the Newton-Raphson algorithm. Details can be found in Appendix C. The liquid
 199 brine pressure p_l and the CO_2 -rich phase pressure p_g are selected as independent variables.
 200 The rest of variables can be explicitly expressed as functions of p_l and p_g through the con-
 201 stitutive equations and the equations of state. This selection of independent variables is con-
 202 venient in dealing with phase appearance and disappearance [Bourgeat *et al.*, 2010; Angelini
 203 *et al.*, 2011; Ern and Mozolevski, 2012; Neumann *et al.*, 2013; Saaltink *et al.*, 2013]. The
 204 time step is chosen to satisfy the Courant–Friedrichs–Lewy (CFL) condition, i.e., for any
 205 grid cell of the domain and flow direction we impose that,

$$\frac{qS\Delta t}{\phi V_c} = Cu, \quad q = \max(q_l, q_g), \quad (14)$$

206 where q is the maximum flux of the two phases, Cu is the courant number fixed to 0.2, S
 207 is the cross-sectional area transverse to the flux, V_c is the grid cell volume, and Δt the time
 208 step. The time step is very sensitive to phase appearance and disappearance. When the sim-
 209 ulation experiences phase appearance/disappearance at a given point, Δt is automatically
 210 reduced to a very small value (e.g., 0.1 second), and then gradually increased following a ge-
 211 ometric progression with a common ratio of 3 until the CFL condition is again satisfied. The
 212 code is capable to simulate injection wells penetrating through different layers. For this, the
 213 mass flux that is transferred to the n th node of the well is given by the pressure difference
 214 between the node and the well as,

$$Q_{g,n}^C = X_g^C \rho_g \frac{2\pi\kappa_n b_n}{\ln(r_e/r_w)} \frac{\kappa_{rg}}{\mu_g} (p_{wg,n} - p_{g,n}), \quad (15)$$

$$Q_{g,n}^H = X_g^H \rho_g \frac{2\pi\kappa_n b_n}{\ln(r_e/r_w)} \frac{\kappa_{rg}}{\mu_g} (p_{wg,n} - p_{g,n}). \quad (16)$$

215 where b_n is the saturated thickness of the cell, r_w and r_e are respectively the well radius
 216 and effective well radius, and $p_{g,n}$ and $p_{wg,n}$ are the gas phase pressure and well pressure

217 at node n , respectively. The well pressure is calculated based on the bottom hole pressure
 218 (p_{bh}) at reference location (z_{bh}) through $p_{wg,n} = p_{bh} + \rho_g g(z_{bh} - z_n)$. Mass balance at the
 219 injection well is written as,

$$Q_{well} = \sum_{n \in N_{well}} Q_{g,n}^C + Q_{g,n}^H, \quad (17)$$

220 where Q_{well} is the total mass injection rate of the CO_2 gas phase, and N_{well} is the number of
 221 grid-cells pierced by the injection well.

222 4 Computational Approach

223 4.1 Model Setup

224 We consider a confined saline formation with an isolated fully-penetrating well centered
 225 in the middle. The system is represented by an axisymmetric model defined by cylin-
 226 drical coordinates (r, φ, z) . The z -axis coincides with the center of the fully-penetrating well.
 227 Figure 1 shows a sketch diagram of the model setup. By symmetry, the solution does not dep-
 228 end on the angular coordinate φ . The top and bottom boundaries are impermeable bound-
 229 aries, and the outer boundary has constant liquid pressure and zero saturation gradient. The
 230 system is initially saturated with brine, which is assumed to be at hydrostatic state, i.e., the
 231 liquid pressure increases downward with a vertical gradient given by the specific gravity of
 232 the liquid phase, $\rho_l g$. The injected $CO_2(g)$ is saturated with water vapor. This is mostly the
 233 case in real applications because dry CO_2 can trigger the dissolution of minerals, such as
 234 halite, and reduce well injectivity. The radius of the injection well is 0.1 [m]. The initial liq-
 235 uid pressure is $p_{li} = 150$ [bar] on the top layer, and the initial gas pressure is $p_{gi} = 1$ [bar]
 236 everywhere. CO_2 is injected at a constant mass injection rate Q_{well} . The parameters adopted
 237 during the simulations are summarized in Table 1. With these parameters, $Q_{well} \approx Q_g^C$ and
 238 Q_g^H is very small ($\sim 0.2\%$). The simulation is terminated when the total injected mass of
 239 CO_2 reaches a value of $M_{inj} = 2.5$ [Mt]. The concentration of $NaCl$ (m_l^S) is fixed to 0.5
 240 [molal] and the temperature (T_c) is 60 [°C]. The axisymmetric model grid discretization con-
 241 sists of N_z layers and N_r coaxial rings around the z -axis. The discretization is uniform in the
 242 vertical direction but increases linearly with r .

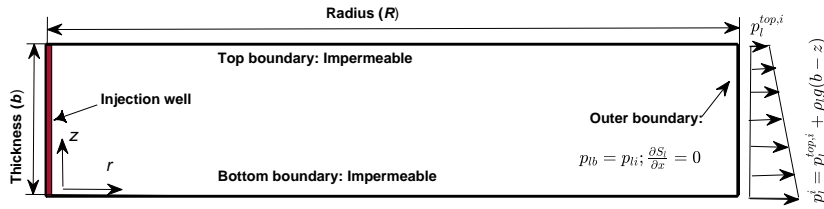


Figure 1: Sketch of the simulation setup.

243 4.2 Model Validation

244 The numerical code is tested against the semi-analytical solution developed by *Nord-*
 245 *botten and Celia* [2006], which provides the vertical location of the interface between the
 246 gaseous CO_2 and the brine phases. The model setup is also represented by Figure 1. How-
 247 ever, in order to satisfy the analytical solution requirements, the permeability, fluid densities,
 248 and fluid viscosities are assumed constant, and the relative permeability is assumed to be lin-
 249 earlyly proportional to saturation. Table 2 provides a summary of the parameters adopted for

Table 1: Summary of the parameters adopted during Monte Carlo simulations.

Parameters	Symbol	Units	Values
Domain size	(R, b)	[m]	(5000, 100)
Grid discretization	(N_r, N_z)	[-]	(100, 100)
Porosity	ϕ	[-]	0.1
Initial liquid pressure	p_{li}	[bar]	150
Initial gas pressure	p_{gi}	[bar]	1
Well radius	r_w	[m]	0.1
Total injection mass	M_{inj}	[Mt]	2.5
Parameter for Eq. (9)	α_p	[bar ⁻¹]	5
Parameter for Eq. (9)	m_p	[-]	0.8
Parameters for Eqs. (11)-(12)	$(\kappa_{rlm}, \kappa_{rgm})$	[-]	(1,1)
Parameters for Eqs. (11)-(12)	(ϵ_p, γ_p)	[-]	(0.5,0.5)
Residual saturations	(S_{lr}, S_{gr})	[-]	(0.2,0)
Hydrodynamic dispersivities	(α_L, α_T)	[m]	(5,1)
Molecular diffusion coefficient	D_m	[m ² .s ⁻¹]	10 ⁻⁹
Salinity	m_l^S	[molal]	0.5
Temperature	T_c	[°C]	60

250 model validation. The table only shows the parameters that have changed from the model
 251 setup listed in Table 1. For comparison purposes, we estimated the location of the interface
 252 by balancing the area of the saturation distribution above and below the interface to preserve
 253 mass balance,

$$z(r) = b - \int_0^b S_g(r, z) dz. \quad (18)$$

254 The comparison between the analytical and numerical solution is shown in Figure 2,
 255 from which we can see that, the numerical result agree well with the theoretical solution.
 256 The size of the $CO_2(g)$ plume given by the numerical solution is slightly smaller than the
 257 analytical solution because the numerical simulation still considers the dissolution of CO_2
 258 into brine.

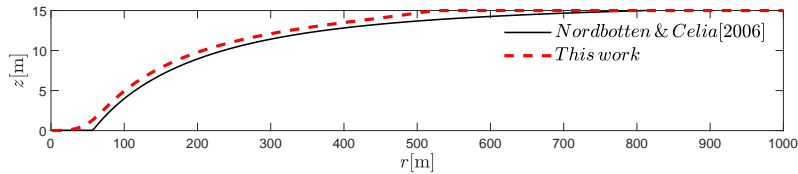

 Figure 2: Comparison of the numerical result with the theoretical solution by *Nordbotten and Celia* [2006].

Table 2: Parameter settings adopted for the model validation.

Parameters	Symbol	Units	Values
Domain size	(R, b)	[m×m]	(2000,15)
Grid discretization	(N_r, N_z)	[-]	(100,20)
Intrinsic permeability	κ	[m ²]	2×10^{-14}
Porosity	ϕ	[-]	0.15
Initial pressures	$(p_l^{top,i}, p_g^i)$	[bar]	(150,10)
Well radius	r_w	[m]	0.1
Injection rate	Q_{well}	[Mt/year]	0.028
Simulation time	T_s	[day]	5194
Viscosities	(μ_l, μ_g)	[mpa·s]	(0.511,0.061)
Densities	(ρ_l, ρ_g)	[kg·m ⁻³]	(1099,733)

4.3 Performance Metric

The analysis of the simulation results is based on the quantification of the total amount of CO_2 dissolved into brine with respect to the total amount of CO_2 injected per unit of time. We therefore define the following performance metric for measuring dissolution efficiency,

$$E(t) = \frac{\mathcal{M}_d(t + \Delta t) - \mathcal{M}_d(t)}{\mathcal{M}_{inj}(t + \Delta t) - \mathcal{M}_{inj}(t)}, \quad (19)$$

where $\mathcal{M}_{inj}(t)$ is the total injected mass of CO_2 at time t , $\mathcal{M}_d(t)$ is the total dissolved mass of CO_2 at time t , and Δt is the time step. Numerically, the mass of dissolved CO_2 into brine is indirectly calculated from the mass of undissolved CO_2 as

$$E(t) = \frac{Q_g^C \Delta t - \sum_i [X_g^C S_g \phi V_c \rho_g]_i^{t+\Delta t} + \sum_i [X_g^C S_g \phi V_c \rho_g]_i^t}{Q_g^C \Delta t}, \quad (20)$$

where V_c is grid cell volume, i denotes the i th grid cells, and Q_g^C is the mass injection rate of CO_2 .

4.4 Stochastic Framework

The simulation approach considers a stochastic description of the natural log of the intrinsic permeability $Y(\mathbf{x}) = \ln \kappa(\mathbf{x})$. The $Y(\mathbf{x})$ random field follows a correlated random space function, characterized by an anisotropic exponential covariance function with mean \bar{Y} , variance σ_Y^2 , vertical correlation length l_v , and a very large horizontal integral scale l_h . We consider that l_h is much larger than the domain size and therefore, for practical purposes, $l_h \rightarrow \infty$. The geometric mean of the permeability is $\kappa_g = 1 \cdot 10^{-13}$ [m²]. The integral scale in the vertical direction l_v is fixed to 5 [m]. We used three different variances σ_Y^2 and six different mass injection rates Q_{well} to analyze the effect of heterogeneity and buoyant forces under different degrees of heterogeneity. Buoyant forces are characterized by the gravity factor G , which is defined as the ratio of gravity forces resulting from fluid density differences to the viscous forces [Nordbotten and Celia, 2006], that is,

$$G = \frac{2\pi\Delta\rho\rho_g g k_h b^2}{Q_{well}\mu_l}, \quad (21)$$

280 where $\Delta\rho = \rho_l - \rho_g$, b is the thickness of the formation, and k_h is the effective vertical
 281 permeability, which is the harmonic mean in this case. The density of the fluids and the vis-
 282 cosity slightly change with time during the simulations. Based on this, to estimate the gravity
 283 factor, we chose to use the spatial mean of these properties obtained at the end of the injec-
 284 tion. Synthetic test cases are summarized in Table 3. Larger values of G indicate larger den-
 285 sity differences between the two fluids and therefore a higher potential for vertical segrega-
 286 tion of CO_2 .

287 Random fields are simulated with the following procedure. We first generate 50 equally
 288 likely realizations of a standardized multiGaussian random field $Y_{std}(\mathbf{x})$, characterized by a
 289 zero mean and unit variance, with the Sequential Gaussian Simulation method implemented
 290 in the SGSIM code [Journal and Huijbregts, 1976]. For each test case, these 50 standardized
 291 realizations are rescaled by $Y(\mathbf{x}) = \bar{Y} + \sigma_Y Y_{std}(\mathbf{x})$ to satisfy the target statistical properties. We
 292 then simulate the injection of CO_2 in each realization. The dissolution trapping efficiency
 293 $E(t)$ is then characterized by their statistical moments (mean behavior and coefficient of vari-
 294 ation). A review of typical statistical properties, mass injection rates and inherent gravity
 295 forces from real GCS field applications is shown in Table 4. The parameters adopted in our
 296 simulations in terms of mass injection rates and gravity forces are representative of real field
 297 applications.

Table 3: Statistical properties of the random fields and mass injection rates in the different simu-
 lated cases.

Case	Q_{well} [Mt/y]	κ_g [m ²]	σ_Y^2 [-]	I_v [m]	$\langle G \rangle$ [-]
1	6.92	10^{-13}	0.1	5.0	0.13
2	2.50	10^{-13}	1.0	5.0	0.13
3	1.80	10^{-13}	4.0	5.0	0.13
4	0.69	10^{-13}	0.1	5.0	1.3
5	0.25	10^{-13}	1.0	5.0	1.3
6	0.18	10^{-13}	4.0	5.0	1.3

298 4.5 Upscaling of Permeability

299 Since the scale of heterogeneity is typically smaller than the size of the numerical dis-
 300 cretization used in most groundwater models, numerous authors have investigated whether
 301 one can simplify the flow system by substituting the heterogeneous distribution of κ by a rep-
 302 resentative value. Results in this matter are well established in the literature and reviewed in
 303 several papers and books [e.g., Wen and Gómez-Hernández, 1996; Renard and de Marsily,
 304 1997; Sanchez-Vila et al., 2006]. In particular, it is well-known that the equivalent perme-
 305 ability of a perfectly stratified medium is the arithmetic mean κ_a of the point permeabili-
 306 ties when the flow is parallel to the stratification and the harmonic mean κ_h when the flow is
 307 perpendicular to the strata. In our system, that is to say that the equivalent permeability is a
 308 second-order symmetric tensor exactly given by

$$\mathbf{K}^e = \begin{bmatrix} \kappa_a & 0 \\ 0 & \kappa_h \end{bmatrix}. \quad (22)$$

309 In this context, this work also evaluates the effect of upscaling permeability on CO_2
 310 dissolution. To achieve this, for each realization of the $Y(\mathbf{x})$ field and test case, we also sim-
 311 ulate the injection of CO_2 assuming that the system is homogeneous and characterized by an

Table 4: Review of formation statistical properties, mass injection rates and gravity forces from real geological carbon sequestration field sites.

Reservoir	Changhua Coastal Industrial Park ¹	Buzzard's Bench ²	Ordos Basin ³	Sleipner ⁴	Tubåen ⁵	In Salah ⁶
Location	Taiwan	US	China	Norway	Norway	Algeria
Depth [m]	~2220	~2025	~1845	~950	~2470	~1860
Thickness [m]	~1000	~150	~290	~300	~60	~20
κ_g [m ²]	9.8×10^{-15}	2.6×10^{-14}	2.7×10^{-16}	1×10^{-12}	5×10^{-13}	1×10^{-14}
σ_Y^2 [-]	6.9^a	5.5^b	2.9^a	10.6^a	5.5^b	-
ϕ [-]	0.16	0.16	0.11	0.35	0.13	0.15
m_l^S [molal]	0.5	0.3	0.3	0.6	2.4	-
Q_{well} [Mt/year]	1.0	1.87	0.1	0.84	0.77	1.0
G [-]	0.07	0.03	0.04	$< 10^{-3}$	1.12	0.002

Reference: ¹Sung et al. [2014], ²Xiao et al. [2019], ³Wang et al. [2016], ⁴Jing et al. [2019], ⁵Arts et al. [2008] and ⁶Michael et al. [2010], ⁵Maldal and Tappel [2004] and ⁶Grude et al. [2013], and ⁶Mathieson et al. [2009, 2011].

^a calculated from log data. ^b calculated from $\sigma_Y^2 \approx R^2/3$, where $R = \log(\kappa_{max}/\kappa_{min})$, as given by Fogg and Zhang [2016].

312 equivalent anisotropic permeability tensor given by \mathbf{K}^e . The rest of the parameters are kept
313 the same.

314 5 Results

315 To facilitate the interpretation, results are presented using dimensionless variables,
316 defined according to Nordbotten and Celia [2006], Silin et al. [2009] and Zhao et al. [2014]
317 as

$$318 \quad t^* = \frac{t}{t_c}, \quad \zeta = \frac{z}{b}, \quad \xi = \frac{r}{\ell}, \quad S_{ge} = \frac{S_g - S_{gr}}{1 - S_{tr} - S_{gr}}, \quad (23)$$

318 where b is the thickness of the geological formation, S_{ge} is the effective gas saturation, and
319 t_c and ℓ are the characteristic time and length scales, respectively defined as

$$320 \quad t_c = \frac{\phi \mu_l b}{\Delta \rho g \kappa_g}, \quad \ell^2 = \frac{M_{inj}}{2\pi \phi \rho_g b}. \quad (24)$$

320 In accordance with Zhao et al. [2014], t_c is an approximate estimate of the time needed
321 for the CO_2 to migrate from the bottom of the formation to the top due to buoyant forces. ℓ is
322 a measure of the radial penetration of CO_2 due to advection only.

323 5.1 Effect of Heterogeneity and Buoyant Forces

324 In this section, we present the effect of heterogeneity and buoyant forces, and their inter-
325 play, on CO_2 dissolution. Figures 3 and 4 show the temporal evolution of the ensemble
326 average of dissolution efficiency and its uncertainty (expressed by the coefficient of varia-
327 tion) for a relatively small and large gravity factor, respectively. In all cases, the temporal
328 evolution exhibits two clear dissolution regimes, characterized by the characteristic time of
329 gravity segregation t_c . At early times ($t < t_c$), gravity segregation controls CO_2 migration,
330 and dissolution efficiency strongly declines with time. After this, for $t > t_c$, when grav-

ity segregation has already developed, the less dense $CO_2(g)$ is overriding the brine, and $CO_2(g)$ plume is mostly spreading laterally. At this point, dissolution efficiency reaches a quasi steady-state behavior with a clear asymptotic value. The decline of dissolution efficiency is attributed to the following. At the very beginning, all the injected CO_2 dissolves into the brine (dissolution efficiency is 100%) until brine becomes saturated and the gas phase appears. After this, the rising of $CO_2(g)$ due to buoyant forces enhances the contact between the brine and gas phases, favoring the mixing between them and therefore dissolution. This process decays with the segregation of $CO_2(g)$ at the top of the formation. After this, $CO_2(g)$ is forced to move laterally by viscous forces, which leads to a steady growth of the interface and thus dissolution efficiency.

Results show that dissolution efficiency generally increases with σ_Y^2 . This effect is more pronounced when the gravity factor is relatively small ($\langle G \rangle = 0.13$). In order to visually understand this effect, in the left panels of Figures 5 and 6, we present the spatial distribution of $CO_2(g)$ saturation obtained at the end of the injection in a representative realization of the permeability field for different σ_Y^2 and mean gravity factors. Note that, by construction, the underlying heterogeneous structure of the permeability field is the same. Results corroborate the hypothesis that heterogeneity tends to stretch the interface between the gas and liquid phases through preferential channels, increasing the contact between them, and therefore, effectively increasing the mutual solubility between the two phases.

Importantly, results also show that heterogeneity and buoyant forces constitute two important competing factors that control dissolution efficiency. When buoyant forces are relatively low compared to the degree of heterogeneity ($G < \sigma_Y^2$), heterogeneity is the dominant factor and CO_2 migration mostly takes place laterally through high permeability layers, regardless of the buoyant forces. In contrast, when the gravity factor is relatively large compared to the degree of heterogeneity ($G > \sigma_Y^2$), gravity segregation is the dominant process. In this case, vertical segregation is overwhelming and the CO_2 gas plume floats to the top of the formation regardless of the permeability stratification. These features can also be seen in Figures 5 and 6 by contrasting, for instance, the results obtained with $\langle G \rangle = 0.13$ against those with $\langle G \rangle = 1.3$ for $\sigma_Y^2 = 1$. In this case, the CO_2 gas plume tends to segregate on top of the formation for $\langle G \rangle = 1.3$, while preferentially moving through a high permeability layer when $\langle G \rangle = 0.13$. In all cases, when $\sigma_Y^2 = 4$, the CO_2 gas plume preferentially concentrates in the most permeable layer.

Our simulated dissolution efficiency values are consistent with those reported in the literature. When $\langle G \rangle = 1.3$ and $\sigma_Y^2 = 1$, we obtain that the dissolution efficiency is around 20%, which is similar to those reported by *Li et al.* [2017] and *Li et al.* [2018] for a synthetic test case with $G \approx 10^3$ and $\sigma_Y^2 = 1.5$. *Al-Khdheawi et al.* [2017] also reported an average solubility trapping of approximately 20% in several synthetic homogeneous aquifers with $G \approx 68$. Numerical simulations of the Changhua Coastal Industrial Park field site [*Sung et al.*, 2014] reported a dissolution efficiency of 15.6%. Smaller values are also reported in the literature. *Zhou et al.* [2008] and *Zhou et al.* [2010] obtained that approximately 7% of the injected CO_2 dissolves into brine when the gravity factor ranges between 0.7 and 2.2. We attribute this to the high brine salinity used (around 4 [molal]), which reduces the mass fraction of $CO_2(aq)$ in brine to only around 2.5%. Finally, we notice that in agreement with our results, *Zhang et al.* [2017] also concluded that the dissolution efficiency was insensitive to heterogeneity for $G \approx 19$ and σ_Y^2 smaller than 4.5.

The uncertainty associated with dissolution efficiency is shown in the bottom panels of Figures 3 and 4. The temporal evolution of CV_E also exhibits two differentiated regimes characterized by t_c . In general, CV_E increases with time as the dissolution efficiency decreases. At large times, when $t > t_c$, CV_E approaches a relatively constant value. As expected, CV_E is larger when dissolution is controlled by the heterogeneity, i.e., when $\sigma_Y^2 > G$. In this case, we can see that the uncertainty increases with σ_Y^2 . When the process is controlled by the gravity segregation, i.e., $G > \sigma_Y^2$, the uncertainty due to σ_Y^2 is reduced. The reason is that when the system is controlled by buoyant forces, the CO_2 tends to float and

384 segregate on the top of the formation, following more or less the same pattern regardless of
 385 the distribution of permeability. As a result, the variability in permeability is not strongly
 386 transferred to the spatial distribution of CO_2 . This is clearly seen in Figure 6, which shows
 387 that the distribution of gas saturation for $\sigma_Y^2 = 0.1$ and $\sigma_Y^2 = 1.0$ still shared very similar
 388 features.

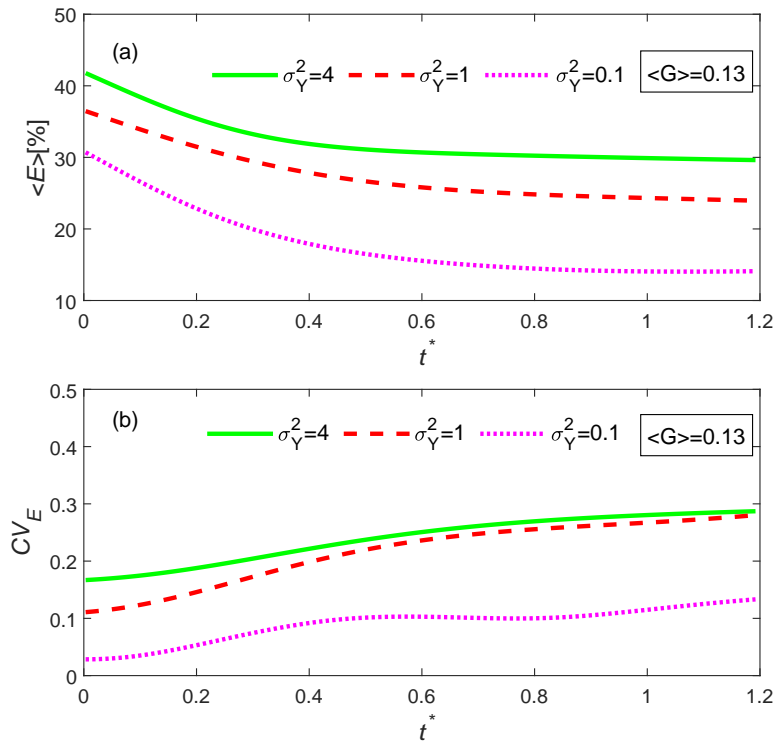


Figure 3: (a) Temporal evolution of the ensemble average dissolution efficiency $\langle E \rangle$ as a function of the degree of heterogeneity for a mean gravity factor of 0.13 (normal injection rate); (b) Temporal evolution of the corresponding coefficient of variation of the dissolution efficiency.

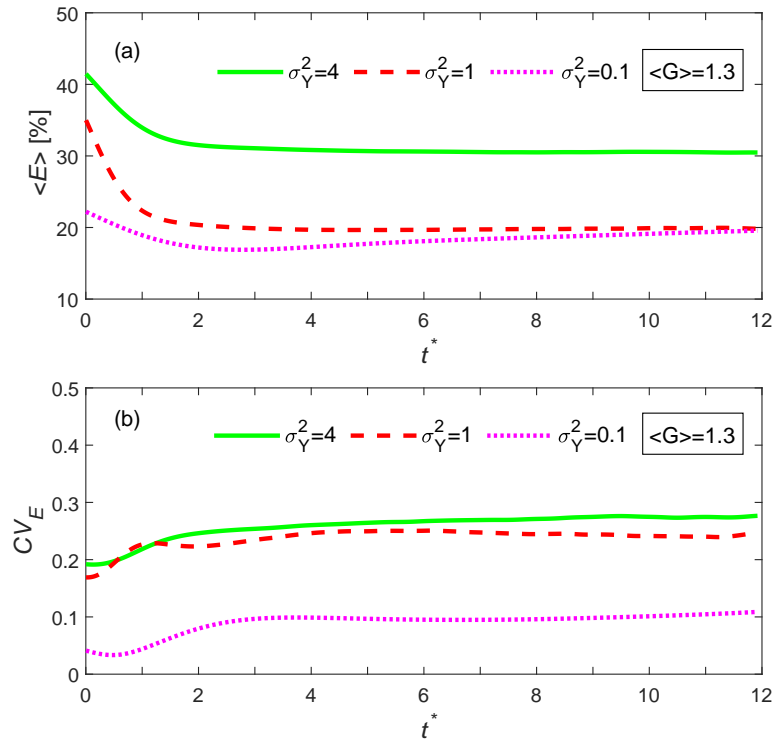


Figure 4: (a) Temporal evolution of the ensemble average dissolution efficiency $\langle E \rangle$ as a function of the degree of heterogeneity for a mean gravity factor of 1.3 (relatively slow injection rate); (b) Temporal evolution of the corresponding coefficient of variation of the dissolution efficiency.

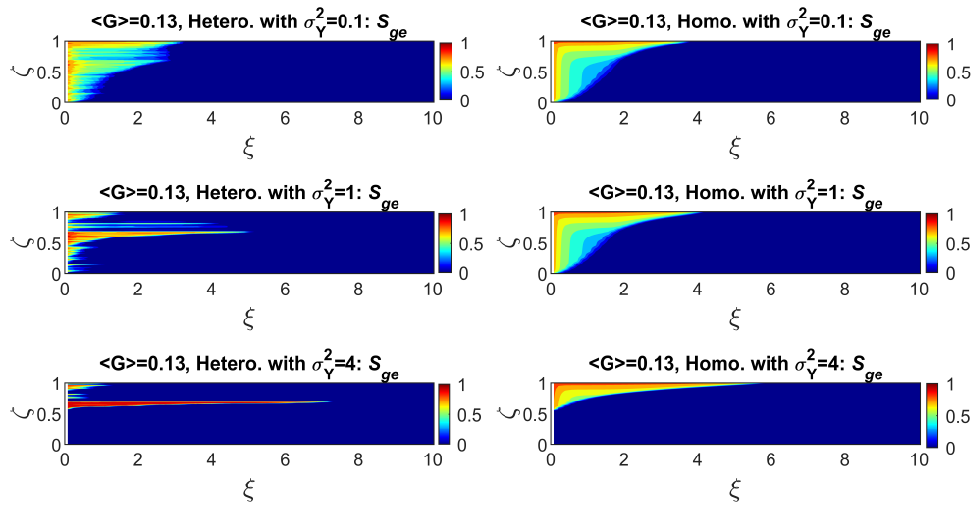


Figure 5: Spatial distribution of $CO_2(g)$ saturation obtained with a large gravity factor at the end of the injection ($t=1.2t_c$): (left column) in a representative heterogeneous realization with different rescaled σ_Y^2 ; and (right column) in the corresponding equivalent homogeneous medium.

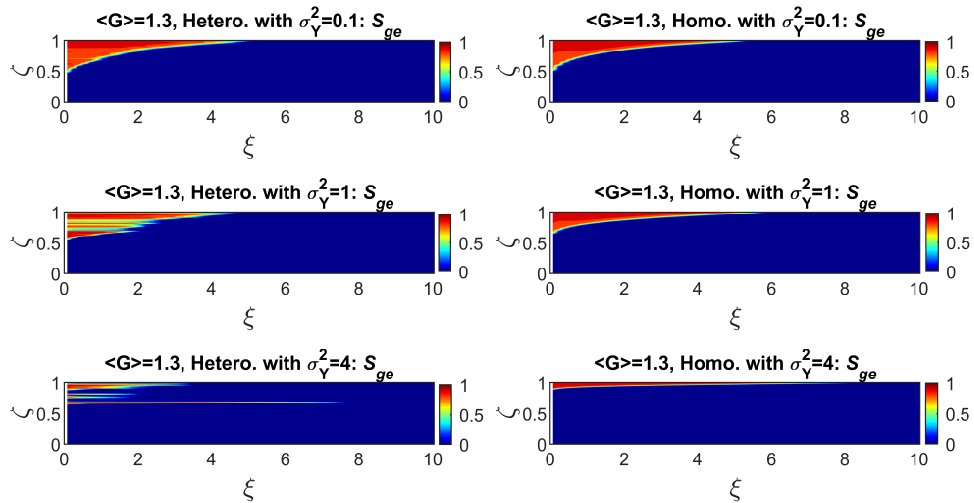


Figure 6: Spatial distribution of $CO_2(g)$ saturation obtained with a small gravity factor at the end of the injection ($t=12t_c$): (left column) in a representative heterogeneous realization with different rescaled σ_Y^2 ; and (right column) in the corresponding equivalent homogeneous medium.

389 5.2 Impact of Upscaling the Permeability

390 In this section, we present the impact that upscaling the permeability has on dissolution
 391 efficiency. To achieve this, for each realization, we substitute the heterogeneous dis-
 392 tribution of permeability by an equivalent homogeneous porous medium, characterized by
 393 an anisotropic permeability tensor defined by equation (22). The dissolution efficiency ob-
 394 tained in the equivalent homogeneous medium is denoted as E_0 . The loss of dissolution effi-
 395 ciency during the upscaling process is expressed by the reduction factor E/E_0 . Figures 7
 396 and 8 show the temporal evolution of the ensemble average of E/E_0 as a function of σ_Y^2
 397 for the two different gravity factors. Results indicate that upscaling can lead to a significant un-
 398 derestimation of dissolution efficiency in heterogeneity-controlled problems, i.e., $G < \sigma_Y^2$.
 399 In these cases, the homogenization of the permeability field does not properly preserve the
 400 interplay between the small-scale spatial variability of permeability and dissolution, which
 401 is characterized by abrupt changes in permeability that enhance the contact between the gas
 402 and brine phases. This is emphasized by the nonlinear nature of the CO_2 -Brine system; the
 403 less viscous $CO_2(g)$ preferentially enters into high permeable layers, increasing the mobil-
 404 ity of $CO_2(g)$ and thus further enhancing the $CO_2(g)$ flux [Rasmussen *et al.*, 2015]. This
 405 nonuniform displacement is also partially attributed to the low capillary entry pressure in the
 406 high permeable layers. For $G = 0.13$ and $\sigma_Y^2 = 4$, we found that dissolution efficiency is re-
 407 duced by a factor close to 1.5 due to upscaling. This reduction factor increases with σ_Y^2 and
 408 decreases with G . When $G > \sigma_Y^2$, the problem is gravity-controlled and the upscaling of
 409 permeability does not introduce an obvious discrepancy in the estimation of the dissolution
 410 efficiency.

411 In order to visually understand the effect of upscaling on dissolution, Figures 5 and 6
 412 compare the spatial distribution of CO_2 gas saturation obtained in heterogeneous field (left
 413 panels) with their corresponding equivalent homogeneous simulations (right panels). Sup-
 414 port information provides additional data on mass fractions. When $G > \sigma_Y^2$, the effect of
 415 gravity segregation controls CO_2 plume migration and the injected $CO_2(g)$ floats to the top
 416 of the formation regardless of stratification. In this case, buoyant forces destroy the action of
 417 heterogeneity, causing an apparent homogenization of the porous media. As a result, the sim-
 418 ulated CO_2 plumes obtained in heterogeneous porous media resembles those of the equiva-
 419 lent homogeneous porous medium. This explains why the reduction factor E/E_0 is close to
 420 1 in this case. When $G < \sigma_Y^2$, gravity segregation is overwhelmed by the stratification of
 421 permeability. In this case, the injected CO_2 mostly enters into high-permeable layers and dis-
 422 solves therein, and the $CO_2(g)$ plume distribution departs from the equivalent homogeneous
 423 medium. In this case, the CO_2 plume fringe looks erratic with CO_2 preferentially flowing
 424 through several highly conductive layers without apparently floating to the top of the forma-
 425 tion. Therefore, small-scale inclusions of high permeable layers fundamentally control the
 426 shape, dynamics and hence the dissolution of CO_2 [Gershenson *et al.*, 2015b,c,a]. In this
 427 case, the reduction factor of dissolution efficiency increases with σ_Y^2 .

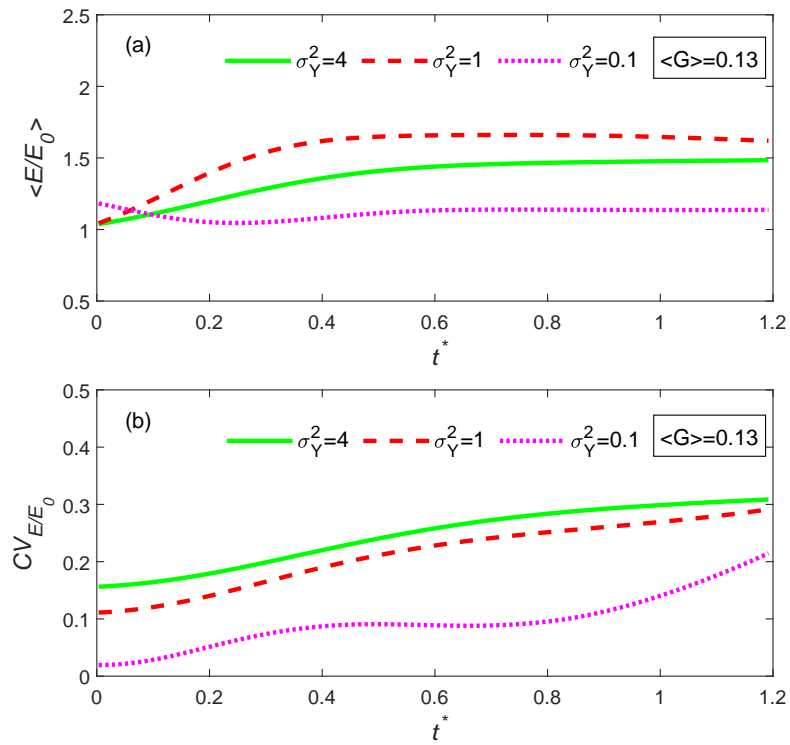


Figure 7: (a) Temporal evolution of the reduction factor $\langle E/E_0 \rangle$ in dissolution efficiency for a mean gravity factor of 0.13 due to the upscaling of permeability; (b) Temporal evolution of the corresponding coefficient of variation of the reduction factor in dissolution efficiency.

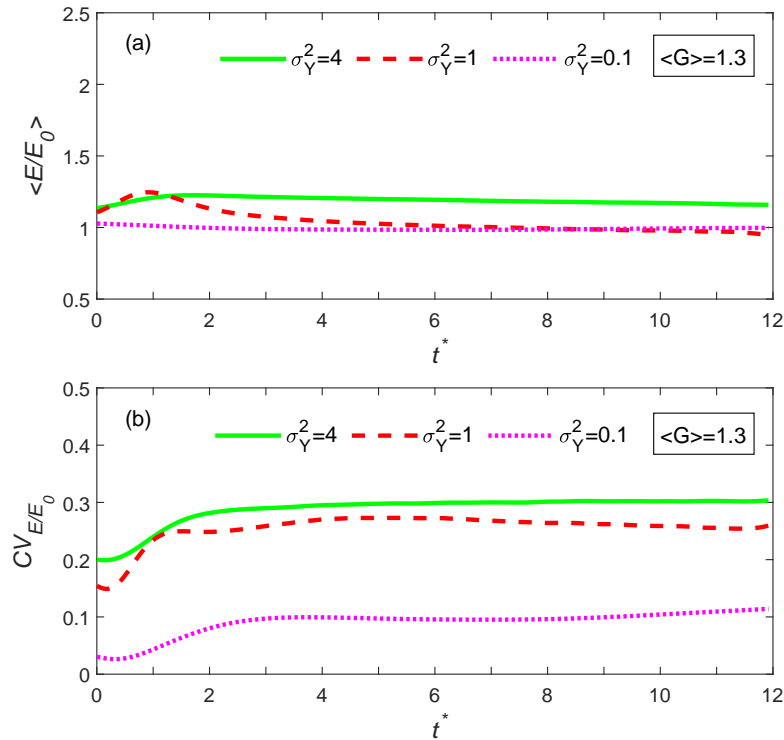


Figure 8: (a) Temporal evolution of the reduction factor $\langle E/E_0 \rangle$ in dissolution efficiency for a mean gravity factor of 1.3 due to the upscaling of permeability; (b) Temporal evolution of the corresponding coefficient of variation of the reduction factor in dissolution efficiency.

5.3 Implications

From a practical point of view, our results indicate that dissolution efficiency can be quite important in complex heterogeneous systems when $G \ll \sigma_Y^2$. Under these conditions, we find that dissolution efficiency can reach values over 30%. At this stage, it is important to highlight that, in most geological formations, the permeability varies in space over 3 orders of magnitude, which means that σ_Y^2 can easily exceed a value of 3 [Fogg and Zhang, 2016]. Consequently, the enhancement of dissolution efficiency observed in our simulations due to small-scale heterogeneity might be the rule rather than the exception in real field settings. To illustrate this, we map the properties associated with the GCS field sites reviewed in Table 4 in a behavior diagram, shown in Figure 9. The $\sigma_Y^2 - G$ diagram has been qualitatively drawn from a limited number of simulations and therefore uncertainties associated with transition lines are expected. Nevertheless, the diagram clearly shows that most field sites are heterogeneity-controlled, meaning that dissolution efficiency might be larger than expected. This is consistent with Goodman *et al.* [2013] and Gershenson *et al.* [2015a], who suggest that incorporating the small-scale heterogeneity is critical to reproduce GCS processes.

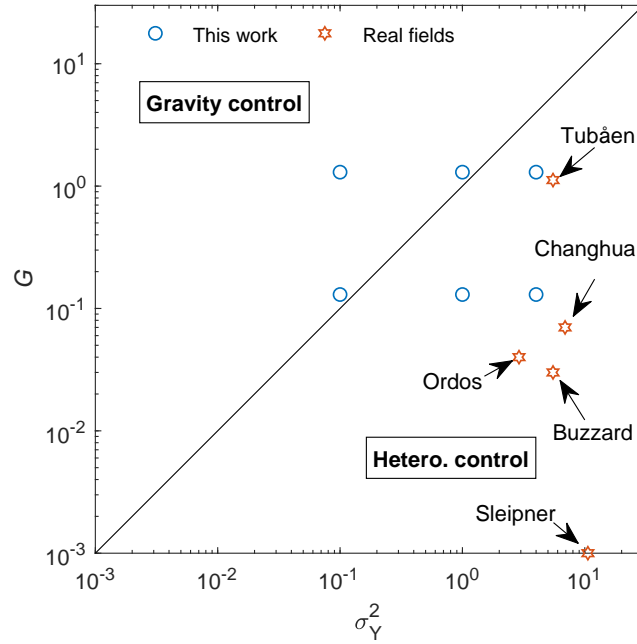


Figure 9: $\sigma_Y^2 - G$ diagram with the simulated test cases, summarized in Table 3, and the GCS field sites reviewed in Table 4.

6 Conclusions

We have investigated dissolution trapping efficiency and its uncertainty during Geological Carbon Sequestration (GCS) in randomly stratified saline formations through a set of Monte Carlo two-phase flow compositional simulations involving the dissolution of CO_2 into brine and evaporation of water into the CO_2 -rich phase under different degrees of heterogeneity and gravity factors. Simulation results have provided a statistical description of dissolution efficiency as well as an examination of the impact of upscaling the permeability in numerical models. The following main findings are highlighted:

1. The interplay between heterogeneity and buoyant forces are shown to control the behavior of CO_2 migration and therefore dissolution efficiency. When buoyant forces G are relatively small compared to the degree of heterogeneity σ_Y^2 , lateral CO_2 migration through high permeability layers dominates the overall behavior and dissolution efficiency increases with σ_Y^2 due to the stretching of the CO_2 plume that enhances mixing. In contrast, when buoyant forces dominate, CO_2 vertical segregation controls the behavior, diminishing the influence of heterogeneity on dissolution. A tentative behavior diagram is proposed with a transition line approximately given by $G = \sigma_Y^2$.
2. The temporal evolution of dissolution efficiency is shown to exhibit two clear regimes characterized by the characteristic segregation time t_c . Dissolution efficiency declines with time until the CO_2 gas phase rises to the top of the formation and segregates from the brine phase. After this, when $t \gg t_c$, CO_2 is forced to move laterally (viscosity forces dominate) and dissolution efficiency reaches an almost asymptotic value.
3. We have shown that the upscaling of permeability leads to an underestimation of the dissolution efficiency. This effect is more pronounced in highly heterogeneous systems with small gravity effects ($G < \sigma_Y^2$) due to the fact that lateral finger-like CO_2 plume is generated in this case following the stratification. On the contrary, when

468 $G > \sigma_Y^2$, a single compact $CO_2(g)$ plume floats to the upper portion of the forma-
 469 tion regardless of heterogeneity, and upscaling is not significantly affected.
 470 4. We have shown that most GCS field sites operate under $G \ll \sigma_Y^2$, meaning that het-
 471 erogeneity typically controls dissolution efficiency in real field settings. Knowing that
 472 most numerical models that simulate CO_2 dissolution cannot properly represent the
 473 small-scale heterogeneity due to an unfeasible discretization of the domain, our results
 474 suggest that dissolution efficiency can be underestimated by a factor close to 1.5.

475 Acknowledgments

476 We acknowledge the help from Oriol Bertran-Oller and Rodrigo Perez in accessing
 477 the TITANI- high performance green computing cluster of the civil engineering school. We
 478 also acknowledge the help from Jan M. Nordbotten for sharing the code for the theoretical
 479 solution. This work was partially supported by the European Commission, through project
 480 MARSOLUT (grant H2020-MSCA-ITN-2018); by the Spanish Ministry of Economy and
 481 Competitiveness, through project MONOPOLIOS (RTI 2018-101990-B-100, MINECO/
 482 FEDER); and by the Catalan Agency for Management of University and Research Grants
 483 through FI 2017 (EMC/2199/2017).

484 A Equilibrium Constants, Fugacity and Activity

485 The equilibrium constants of the two reaction equations are calculated as

$$K^\beta = K^{\beta_0} \exp \frac{(p_l - p^0) \bar{V}_\beta}{RT_c}, \quad (\text{A.1})$$

486 with

$$K^{\beta_0} = 10^{a_\beta + b_\beta T_c + c_\beta T_c^2 + d_\beta T_c^3}, \quad (\text{A.2})$$

487 where, p^0 is the reference pressure (equal to 1 bar), T_c is temperature in $^\circ\text{C}$, \bar{V}_β [$\text{cm}^3 \cdot \text{mol}^{-1}$]
 488 denotes the mean molar volume of pure condensed species β when pressure change from p^0
 489 to p_l . Here, we assume \bar{V}_β is a constant. The parameters for Equation A.2, given in *Spycher*
 490 *et al.* [2003], are listed in Table A.1.

Table A.1: Parameters for equilibrium constants.

β	a_β	b_β	c_β	d_β	\bar{V}_β [$\text{cm}^3 \cdot \text{mol}^{-1}$]
$H_2O_{(g)}$	-2.209	3.097×10^{-2}	-1.098×10^{-4}	2.048×10^{-7}	18.1
$CO_{2(g)}$	1.189	1.304×10^{-2}	-5.446×10^{-5}	0	32.6

491 The fugacity and activity are calculated as

$$f_g^\beta = F^\beta x_g^\beta \frac{p_g}{p^0}, \quad (\text{A.3})$$

$$a_l^H = x_l^H = 1 - x_l^S - x_l^C, \quad (\text{A.4})$$

$$a_i^C = \gamma'_C m_i^C, \quad (\text{A.5})$$

where F^β is the fugacity coefficient, x_α^β is the molar fraction of the β chemical component in the α phase, γ'_C is the activity coefficient of $CO_2(aq)$ in the liquid phase, and m_i^C is the molality of $CO_2(aq)$ in the liquid phase. Here, the simplified model for water activity, given in Equation (A.4), yields very similar results as the sophisticated Helgeson-Kirkham-Flowers (HKF) model (comparison is not shown). In order to solve Equations (A.3) to (A.5), we need to know the fugacity coefficients $F^{H,C}$ and activity coefficient γ'_C . According to *Spycher et al.* [2003], the fugacity coefficients of the gaseous species are calculated as

$$\begin{aligned} \ln F^\beta = & \ln \frac{V}{V - b^{mix}} + \frac{b^\beta}{V - b^{mix}} - \ln \frac{V + b^{mix}}{V} \frac{2}{RT_k^{1.5} b^{mix}} \sum_{\beta'=C,H} (x_g^\beta a^{\beta'-\beta}) \\ & + \frac{a^{mix} - b^\beta}{RT_k^{1.5} (b^{mix})^2} \left(\ln \frac{V + b^{mix}}{V} - \frac{b^{mix}}{V + b^{mix}} \right) - \ln \frac{p_g V}{RT_k}, \end{aligned} \quad (\text{A.6})$$

where $\beta = (C, H, mix)$ represents the species CO_2 , H_2O and $CO_2 - H_2O$ mixture, respectively, V is obtained from Equation (A.7). Assuming infinity dilution, $a^{mix} = a^C$ and $b^{mix} = b^C$. a^C and b^C are defined by (A.8) and (A.9), respectively. $b^H = 1.818 \times 10^{-5} [\text{m}^3 \cdot \text{mol}^{-1}]$ and $a^{H-C} = 7.89 [\text{Pa} \cdot \text{m}^6 \cdot \text{K}^{0.5} \cdot \text{mol}^{-2}]$. We assume infinite dilution of water vapor, i.e., $x_g^H = 0$. So, we do not need a^H . The molar volume of CO_2 phase ($V [\text{m}^3 \cdot \text{mol}^{-1}]$) is obtained by solving the cubic form of Redlich-Kwong equation [*Redlich and Kwong*, 1949],

$$V^3 - V^2 \left(\frac{RT_k}{p_g} \right) - V \left(\frac{RT_k b}{p_g} - \frac{a}{p_g T_k^{0.5}} + b^2 \right) - \left(\frac{ab}{p_g T_k^{0.5}} \right) = 0, \quad (\text{A.7})$$

where $a [\text{bar} \cdot \text{cm}^6 \cdot \text{K}^{0.5} \cdot \text{mol}^{-2}]$ and $b [\text{cm}^3 \cdot \text{mol}^{-1}]$ are, respectively, the intermolecular attraction and repulsion of the CO_2 -rich phase. For simplification, assuming infinite dilution of water vapor, we use the intermolecular attraction and repulsion of pure CO_2 , a^C and b^C , to represent a and b . This is reasonable because the fraction of water vapor in the CO_2 rich phase is usually less than 1%. Therefore, according to *Spycher et al.* [2003], we have

$$a = a^C = 7.54 \times 10^7 - 4.13 \times 10^4 T_k, \quad (\text{A.8})$$

and

$$b = b^C = 27.8. \quad (\text{A.9})$$

Here, we note that Equation (A.7) may have more than one real solutions. The selection of the value depends on which phase –gas or liquid– is more stable. If the more stable phase is gas then we choose the maximum value. Otherwise, we choose the minimum value. To determine which phase is more stable, we need to calculate two works (w_1 and w_2) for phase transition,

$$w_1 = p_g (V_{max} - V_{min}), \quad (\text{A.10})$$

and

$$w_2 = RT \ln \frac{V_{max} - b}{V_{min} - b} + \frac{a}{T^{0.5} b} \ln \frac{(V_{max} + b) V_{min}}{(V_{min} + b) V_{max}}, \quad (\text{A.11})$$

517 If $w_2 \geq w_1$, then gaseous state is more stable and we choose V_{max} . Otherwise, we
 518 take V_{min} . The activity coefficient of aqueous CO_2 (γ'_C), given by *Duan and Sun* [2003], is
 519 estimated as

$$\gamma'_C = 2\lambda \left(m_l^{Na} + m_l^K + 2m_l^{Mg} \right) + \xi m_{Cl} \left(m_l^{Na} + m_l^K + m_l^{Ca} + m_l^{Mg} \right) - 0.07m_l^{SO_4}, \quad (A.12)$$

where

$$\begin{aligned} \lambda = & -0.411370585 + 6.07632013^{-4}T_k + \frac{97.5347708}{T_k} - \frac{0.0237622469 p_l}{T_k} \times 10^{-5} \\ & + \frac{0.0170656236 p_l}{630 - T_k} \times 10^{-5} + 1.41335834 \times 10^{-5}T_k \ln \left(p_l \times 10^{-5} \right) \end{aligned} \quad (A.13)$$

and

$$\begin{aligned} \xi = & 3.36389723 \times 10^{-4} - 1.98298980 \times 10^{-5}T_k + \frac{2.12220830 \times 10^{-3} p_l}{T_k} \times 10^{-5} \\ & - \frac{5.24873303 \times 10^{-3} p_l}{630 - T_k} \times 10^{-5}. \end{aligned} \quad (A.14)$$

520 Here, p_l is in Pa and T_k is in K. We note that this activity coefficient is not a *true* coefficient
 521 but a coefficient defined as the ratio of molality of $CO_2(aq)$ in pure water ($m_l^{C_0}$) to molality
 522 of CO_2 in brine (m_l^C) at same temperature and pressure,

$$\gamma'_{CO_2} = m_l^{C_0} / m_l^C. \quad (A.15)$$

523 **B *Spycher and Pruess* [2005] Model for Mutual Solubility**

524 The chemical reactions (1) and (2) are solved with the *Spycher and Pruess* [2005]
 525 model, which can calculate the mutual solubility between gas and high-salinity brine at high
 526 pressures and reservoir temperatures. *Spycher and Pruess* [2005] model is given as follows.
 527 When reaction is at equilibrium we have

$$x_g^H = \frac{K^H a_l^H}{F^H p_g} \quad (B.1)$$

528 and

$$x_l^C = \frac{F^C (1 - x_g^H) p_g}{55.508 \gamma'_{CO_2} K^C}. \quad (B.2)$$

529 Setting

$$A = \frac{K^H}{F^H p_g} \quad (B.3)$$

530 and

$$B = \frac{K^C p_g}{55.508 \gamma'_{CO_2} K^C}, \quad (B.4)$$

531 the mutual solubilities are then explicitly given as

$$x_g^H = \frac{1 - B - x_l^S}{\frac{1}{A} - B} \quad (\text{B.5})$$

532 and

$$x_l^C = B(1 - x_g^H). \quad (\text{B.6})$$

533 It is better to use salt molality instead of mole fraction because salt molality is inde-
 534 pendent of CO_2 solubility. Therefore, we change Equation (B.5) by

$$x_g^H = \frac{55.508(1 - B)}{\left(\frac{1}{A} - B\right)(\nu m_l^S + 55.508) + B\nu m_l^S}, \quad (\text{B.7})$$

535 where ν is the stoichiometric number of ions in the salt (e.g., 2 for $NaCl$ and 3 for $MgCl_2$).
 536 The detailed derivation of Equation (B.7) can be found in *Spycher and Pruess* [2005]. With
 537 Equations (B.7) and (B.6), we can explicitly update the mole fractions in both liquid brine
 538 and gaseous CO_2 -rich phases. Note that in the transport equations the concentrations are
 539 given as mass fractions, while mole fractions are used to solve the mutual solubility. We can
 540 change the mole fractions into mass fractions with

$$X_g^H = \frac{18.015x_g^H}{18.015x_g^H + 44.01(1 - x_g^H)} \quad (\text{B.8})$$

541 and

$$X_l^C = \frac{44.01x_l^C}{18.015(1 - x_l^C)(1 + 0.05844m_l^S) + 44.01x_l^C}. \quad (\text{B.9})$$

542 Herein, because we use the activity coefficient of $CO_2(aq)$ given by *Duan and Sun*
 543 [2003], which is not ‘true’ activity coefficient, we need to slightly change the aforementioned
 544 steps [*Hassanzadeh et al.*, 2008].

545 C Numerical Discretization and Newton-Raphson Iteration

546 The governing equations (3) and (4) are discretized in space with the finite difference
 547 method. Time is discretized with fully implicit method. The discretization form is given as

$$\begin{aligned} \mathcal{F}_{1,2} = & V_c \cdot \sum_{\alpha=l,g} \left[\frac{(\phi S_\alpha \rho_\alpha X_\alpha^{H,C})^{t+\Delta t} - (\phi S_\alpha \rho_\alpha X_\alpha^{H,C})^t}{\Delta t} \right] \\ & + \left[\sum_i \left(\mathcal{S}_i \cdot \sum_{\alpha=l,g} (\rho_\alpha X_\alpha^{H,C} \mathbf{q}_\alpha)^{t+\Delta t} \right) - \sum_i \left(\mathcal{S}_i \cdot \sum_{\alpha=l,g} (\phi S_\alpha \mathbf{D}_\alpha \rho_\alpha \nabla X_\alpha^{H,C})^{t+\Delta t} \right) \right] \\ & - (Q_g^{H,C})^{t+\Delta t}, \end{aligned} \quad (\text{C.1})$$

548 where V_c is the volume the grid, \mathcal{S}_i is the i th surface of the grid, and Δt is the time step.
 549 The flux \mathbf{q}_α is calculated with the two-point approximation of Darcy’s law, and the upwind

550 method is used to calculate fluid property [Lie, 2019]. We then write the governing equations
 551 in compact form,

$$\mathcal{F}(\mathbf{x}) = \mathbf{0}, \quad (\text{C.2})$$

552 where

$$[\mathcal{F}] = \begin{bmatrix} \mathcal{F}_1 \\ \mathcal{F}_2 \\ \mathcal{F}_W \end{bmatrix}, [\mathbf{x}] = \begin{bmatrix} p_l \\ p_g \\ p_{bh} \end{bmatrix}. \quad (\text{C.3})$$

553 Here, \mathcal{F}_W expresses the mass balance at the injection well, which is written as

$$0 = \mathcal{F}_W = \left(\sum_{n \in N_{well}} Q_{g,n}^C + Q_{g,n}^H \right) - Q_{well}. \quad (\text{C.4})$$

554 From this, the Newton-Raphson algorithm is written as

$$\frac{\partial [\mathcal{F}]^{t+\Delta t, k}}{\partial \mathbf{x}} [\delta \mathbf{x}]^{t+\Delta t, k} = -[\mathcal{F}]^{t+\Delta t, k}, \quad (\text{C.5})$$

555 where the superscript k denotes the iteration step, and the Jacobian matrix is

$$\left[\frac{\partial \mathcal{F}}{\partial \mathbf{x}} \right]^{t+\Delta t, k} = \begin{bmatrix} \frac{\partial \mathcal{F}_1}{\partial p_l} & \frac{\partial \mathcal{F}_1}{\partial p_g} & \frac{\partial \mathcal{F}_1}{\partial p_{bh}} \\ \frac{\partial \mathcal{F}_2}{\partial p_l} & \frac{\partial \mathcal{F}_2}{\partial p_g} & \frac{\partial \mathcal{F}_2}{\partial p_{bh}} \\ \frac{\partial \mathcal{F}_W}{\partial p_l} & \frac{\partial \mathcal{F}_W}{\partial p_g} & \frac{\partial \mathcal{F}_W}{\partial p_{bh}} \end{bmatrix}^{t+\Delta t, k} = \begin{bmatrix} M_{11} & M_{12} & M_{1W} \\ M_{21} & M_{22} & M_{2W} \\ M_{W1} & M_{W2} & M_{WW} \end{bmatrix}^{t+\Delta t, k} = \mathbf{M}^{t+\Delta t, k}. \quad (\text{C.6})$$

556 Having obtained $[\delta \mathbf{x}]^{t+\Delta t, k}$ with Equation (C.5), we can update $[\mathbf{x}]^{t+\Delta t, k}$ according to

$$[\mathbf{x}]^{t+\Delta t, k+1} = [\mathbf{x}]^{t+\Delta t, k} + [\delta \mathbf{x}]^{t+\Delta t, k}. \quad (\text{C.7})$$

557 The Newton-Raphson iteration is terminated if the maximum change of the gas and
 558 liquid pressures is smaller than the tolerance value ϵ_p ($\sim 10^{-5}$ pa), or if the maximum error
 559 is smaller than the tolerance value ϵ_{err} ($\sim 10^{-12}$). The time step is reduced to a very small
 560 value (e.g., 0.1 second) if the Newton-Raphson iteration does not converge at maximum al-
 561 lowed number of iteration N_{kmax} .

562 References

- 563 Al-Khdheawi, E. A., S. Vialle, A. Barifcani, M. Sarmadivaleh, and S. Iglauer (2017), In-
 564 fluence of co2-wettability on co2 migration and trapping capacity in deep saline aquifers,
 565 *Greenhouse Gases: Science and Technology*, 7(2), 328–338.
- 566 Angelini, O., C. Chavant, E. Chénier, R. Eymard, and S. Granet (2011), Finite volume ap-
 567 proximation of a diffusion-dissolution model and application to nuclear waste storage, in
 568 *Mathematics and Computers in Simulation*, doi:10.1016/j.matcom.2010.12.016.
- 569 Arts, R., A. Chadwick, O. Eiken, S. Thibeau, and S. Nooner (2008), Ten years' experience of
 570 monitoring co2 injection in the utsira sand at sleipner, offshore norway, *First break*, 26(1).
- 571 Bachu, S., D. Bonijoly, J. Bradshaw, R. Burruss, S. Holloway, N. P. Christensen, and O. M.
 572 Mathiassen (2007), Co2 storage capacity estimation: Methodology and gaps, *Interna-*
 573 *tional Journal of Greenhouse Gas Control*, 1(4), 430 – 443, doi:https://doi.org/10.1016/
 574 S1750-5836(07)00086-2.

- 575 Bandara, U. C., A. M. Tartakovsky, and B. J. Palmer (2011), Pore-scale study of capillary
576 trapping mechanism during CO₂ injection in geological formations, *International Journal*
577 *of Greenhouse Gas Control*, doi:10.1016/j.ijggc.2011.08.014.
- 578 Birkholzer, J. T., Q. Zhou, and C. F. Tsang (2009), Large-scale impact of CO₂ storage in
579 deep saline aquifers: A sensitivity study on pressure response in stratified systems, *In-*
580 *ternational Journal of Greenhouse Gas Control*, doi:10.1016/j.ijggc.2008.08.002.
- 581 Bourgeat, A., M. Jurak, and F. Smari (2010), Modelling and numerical simulation of gas mi-
582 gration in a nuclear waste repository.
- 583 Bryant, S. L., S. Lakshminarasimhan, and G. A. Pope (2008), Buoyancy-dominated multi-
584 phase flow and its effect on geological sequestration of CO₂, *SPE Journal*, doi:10.2118/
585 99938-PA.
- 586 Chadwick, R., and D. Noy (2010a), History-matching flow simulations and time-lapse seis-
587 mic data from the sleipner co₂ plume, in *Geological Society, London, petroleum geology*
588 *conference series*, vol. 7, pp. 1171–1182, Geological Society of London.
- 589 Chadwick, R. A., and D. J. Noy (2010b), History-matching flow simulations and time-lapse
590 seismic data from the Sleipner CO₂ plume, in *Petroleum Geology Conference Proceed-*
591 *ings*, doi:10.1144/0071171.
- 592 Chadwick, R. A., R. Arts, O. Eiken, G. A. Kirby, E. Lindeberg, and P. Zweigel (2004), 4D
593 Seismic Imaging of an Injected CO₂ Plume at the Sleipner Field, Central North Sea, *Geo-*
594 *logical Society Memoir*, doi:10.1144/GSL.MEM.2004.029.01.29.
- 595 Chadwick, R. A., R. Arts, and O. Eiken (2005), 4D seismic quantification of a growing
596 CO₂ plume at Sleipner, North Sea, in *Petroleum Geology Conference Proceedings*, doi:
597 10.1144/0061385.
- 598 Cottin, C., H. Bodiguel, and A. Colin (2010), Drainage in two-dimensional porous media:
599 From capillary fingering to viscous flow, *Physical Review E - Statistical, Nonlinear, and*
600 *Soft Matter Physics*, doi:10.1103/PhysRevE.82.046315.
- 601 Dentz, M., T. Le Borgne, A. Englert, and B. Bijeljic (2011), Mixing, spreading and reaction
602 in heterogeneous media: A brief review, doi:10.1016/j.jconhyd.2010.05.002.
- 603 Doughty, C., and K. Pruess (2004), Modeling Supercritical Carbon Dioxide Injection in Het-
604 erogeneous Porous Media, *Vadose Zone Journal*, doi:10.2113/3.3.837.
- 605 Doughty, C., K. Pruess, S. M. Benson, S. D. Hovorka, P. R. Knox, and C. T. Green (2001),
606 Capacity investigation of brine-bearing sands of the frio formation for geologic sequestra-
607 tion of CO₂, *GCCC Texts and Reports*.
- 608 Duan, Z., and R. Sun (2003), An improved model calculating CO₂ solubility in pure water
609 and aqueous NaCl solutions from 273 to 533 K and from 0 to 2000 bar, *Chemical Geol-*
610 *ogy*, doi:10.1016/S0009-2541(02)00263-2.
- 611 Ern, A., and I. Mozolevski (2012), Discontinuous Galerkin method for two-component
612 liquid-gas porous media flows, *Computational Geosciences*, doi:10.1007/
613 s10596-012-9277-3.
- 614 Fernández-García, D., X. Sánchez-Vila, and A. Guadagnini (2008), Reaction rates and ef-
615 fective parameters in stratified aquifers, *Advances in Water Resources*, doi:10.1016/j.
616 advwatres.2008.07.001.
- 617 Flett, M., R. Gurton, and I. Taggart (2004), The function of gas-water relative permeability
618 hysteresis in the sequestration of carbon dioxide in saline formations, in *SPE Asia Pacific*
619 *Oil and Gas Conference and Exhibition, APOGCE*, doi:10.2118/88485-ms.
- 620 Fogg, G. E., and Y. Zhang (2016), Debates-stochastic subsurface hydrology from theory to
621 practice: A geologic perspective, *Water Resources Research*, 52(12), 9235–9245, doi:
622 https://doi.org/10.1002/2016WR019699.
- 623 Garcia, J. E. (2003), Fluid Dynamics of Carbon Dioxide Disposal into Saline Aquifers, *TH:*
624 *Thesis (Ph.D.); Submitted to the University of California, Berkeley, CA (US); PBD: 18*
625 *Dec 2003*.
- 626 Gasda, S. E., J. M. Nordbotten, and M. A. Celia (2012), Application of simplified models
627 to CO₂ migration and immobilization in large-scale geological systems, *International*
628 *Journal of Greenhouse Gas Control*, doi:10.1016/j.ijggc.2012.03.001.

- 629 Gershenson, N. I., R. W. Ritzi, D. F. Dominic, M. Soltanian, E. Mehnert, and R. T. Okwen
630 (2015a), Influence of small-scale fluvial architecture on CO₂ trapping processes in deep
631 brine reservoirs, *Water Resources Research*, doi:10.1002/2015WR017638.
- 632 Gershenson, N. I., M. Soltanian, R. W. Ritzi Jr, and D. F. Dominic (2015b), Understanding
633 the impact of open-framework conglomerates on water–oil displacements: the victor inter-
634 val of the ivishak reservoir, prudhoe bay field, alaska.
- 635 Gershenson, N. I., M. R. Soltanian, R. W. Ritzi Jr, D. F. Dominic, D. Keefer, E. Shaffer, and
636 B. Storsved (2015c), How does the connectivity of open-framework conglomerates within
637 multi-scale hierarchical fluvial architecture affect oil-sweep efficiency in waterflooding?,
638 *Geosphere*, 11(6), 2049–2066.
- 639 Goodman, A., G. Bromhal, B. Strazisar, T. Rodosta, W. F. Guthrie, D. Allen, and G. Guthrie
640 (2013), Comparison of methods for geologic storage of carbon dioxide in saline forma-
641 tions, *International Journal of Greenhouse Gas Control*, 18, 329–342.
- 642 Green, C. P., and J. Ennis-King (2010), Effect of vertical heterogeneity on long-term
643 migration of CO₂ in saline formations, *Transport in Porous Media*, doi:10.1007/
644 s11242-009-9498-7.
- 645 Gregersen, U. (1998), Upper Cenozoic channels and fans on 3D seismic data in the northern
646 Norwegian North Sea, *Petroleum Geoscience*, doi:10.1144/petgeo.4.1.67.
- 647 Grude, S., M. Landrø, and B. Osdal (2013), Time-lapse pressure–saturation discrimination
648 for co₂ storage at the snøhvit field, *International Journal of Greenhouse Gas Control*, 19,
649 369–378.
- 650 Gunter, W. D., S. Bachu, and S. Benson (2004), The role of hydrogeological and geochem-
651 ical trapping in sedimentary basins for secure geological storage of carbon dioxide, *Geo-*
652 *logical Society, London, Special Publications*, 233(1), 129–145.
- 653 Hassanzadeh, H., M. Pooladi-Darvish, A. M. Elsharkawy, D. W. Keith, and Y. Leonenko
654 (2008), Predicting PVT data for CO₂-brine mixtures for black-oil simulation of CO₂
655 geological storage, *International Journal of Greenhouse Gas Control*, doi:10.1016/
656 S1750-5836(07)00010-2.
- 657 Hayek, M., E. Mouche, and C. Mügler (2009), Modeling vertical stratification of CO₂ in-
658 jected into a deep layered aquifer, *Advances in Water Resources*, doi:10.1016/j.advwatres.
659 2008.12.009.
- 660 Henri, C. V., D. Fernández-García, and F. P. J. de Barros (2015), Probabilistic human health
661 risk assessment of degradation-related chemical mixtures in heterogeneous aquifers: Risk
662 statistics, hot spots, and preferential channels, *Water Resources Research*, 51(6), 4086–
663 4108, doi:10.1002/2014WR016717.
- 664 Humez, P., P. Audigane, J. Lions, C. Chiaberge, and G. Bellenfant (2011), Modeling of CO₂
665 Leakage up Through an Abandoned Well from Deep Saline Aquifer to Shallow Fresh
666 Groundwaters, *Transport in Porous Media*, doi:10.1007/s11242-011-9801-2.
- 667 Ide, S. T., K. Jessen, and F. M. Orr Jr (2007), Storage of co₂ in saline aquifers: Effects of
668 gravity, viscous, and capillary forces on amount and timing of trapping, *International*
669 *Journal of Greenhouse Gas Control*, 1(4), 481–491.
- 670 IPCC (2005), Underground Geologic Storage (Chapter 5), in *IPCC Special Report on Car-*
671 *bon Dioxide Capture and Storage*.
- 672 IPCC (2008), Climate change 2007: mitigation of climate change: contribution of Working
673 Group III to the Fourth Assessment Report of the Intergovernmental Panel on Climate
674 Change, *Choice Reviews Online*, doi:10.5860/choice.45-5006.
- 675 Jing, J., Z. Tang, Y. Yang, and L. Ma (2019), Impact of formation slope and fault on co₂
676 storage efficiency and containment at the shenhua co₂ geological storage site in the ordos
677 basin, china, *International Journal of Greenhouse Gas Control*, 88, 209–225.
- 678 Journel, A., and C. Huijbregts (1976), Mining geostatistics.
- 679 Juanes, R., E. J. Spiteri, F. M. Orr, and M. J. Blunt (2006), Impact of relative perme-
680 ability hysteresis on geological CO₂ storage, *Water Resources Research*, doi:10.1029/
681 2005WR004806.

- 682 Kabera, T., and Y. Li (2011), Impact of co₂ injection in deep saline aquifers: A study on
683 pressure evolution in stratified formation of qianjiang sag, china, *International Journal*
684 *of Chemical Engineering and Applications*, 2(2), 121.
- 685 Knudby, C., and J. Carrera (2005), On the relationship between indicators of geostatistical,
686 flow and transport connectivity, *Advances in Water Resources*, 28(4), 405 – 421, doi:<https://doi.org/10.1016/j.advwatres.2004.09.001>.
- 687
688 Krevor, S., M. J. Blunt, S. M. Benson, C. H. Pentland, C. Reynolds, A. Al-Menhali, and
689 B. Niu (2015), Capillary trapping for geologic carbon dioxide storage - From pore scale
690 physics to field scale implications, *International Journal of Greenhouse Gas Control*, doi:
691 10.1016/j.ijggc.2015.04.006.
- 692 Krevor, S. C., R. Pini, B. Li, and S. M. Benson (2011), Capillary heterogeneity trapping of
693 CO₂ in a sandstone rock at reservoir conditions, *Geophysical Research Letters*, doi:10.
694 1029/2011GL048239.
- 695 Kumar, A., R. Ozah, M. Noh, G. A. Pope, S. Bryant, K. Sepehmooi, and L. W. Lake (2005),
696 Reservoir simulation of CO₂ storage in deep saline aquifers, *SPE Journal*, doi:10.2118/
697 89343-pa.
- 698 Leal, A. M., M. J. Blunt, and T. C. LaForce (2013), A robust and efficient numerical
699 method for multiphase equilibrium calculations: Application to CO₂-brine-rock sys-
700 tems at high temperatures, pressures and salinities, *Advances in Water Resources*, doi:
701 10.1016/j.advwatres.2013.02.006.
- 702 Lee, Y., K. Kim, W. Sung, and I. Yoo (2010), Analysis of the leakage possibility of injected
703 CO₂ in a saline aquifer, *Energy and Fuels*, doi:10.1021/ef100073m.
- 704 Lenormand, R., E. Touboul, and C. Zarcone (1988), Numerical models and experiments on
705 immiscible displacements in porous media, *Journal of Fluid Mechanics*, doi:10.1017/
706 S0022112088000953.
- 707 Li, D., Y. He, H. Zhang, W. Xu, and X. Jiang (2017), A numerical study of the impurity ef-
708 fects on co₂ geological storage in layered formation, *Applied energy*, 199, 107–120.
- 709 Li, D., H. Zhang, Y. Li, W. Xu, and X. Jiang (2018), Effects of n₂ and h₂s binary impurities
710 on co₂ geological storage in stratified formation—a sensitivity study, *Applied energy*, 229,
711 482–492.
- 712 Lie, K.-A. (2019), *An introduction to reservoir simulation using MATLAB/GNU Octave:*
713 *User guide for the MATLAB Reservoir Simulation Toolbox (MRST)*, Cambridge University
714 Press.
- 715 Maldal, T., and I. Tappel (2004), Co₂ underground storage for snøhvit gas field development,
716 *Energy*, 29(9-10), 1403–1411.
- 717 Mathieson, A., I. Wright, D. Roberts, and P. Ringrose (2009), Satellite imaging to monitor
718 co₂ movement at krechba, algeria, *Energy Procedia*, 1(1), 2201–2209.
- 719 Mathieson, A., J. Midgely, I. Wright, N. Saoula, and P. Ringrose (2011), In salah co₂ stor-
720 age jip: Co₂ sequestration monitoring and verification technologies applied at krechba,
721 algeria, *Energy Procedia*, 4, 3596–3603.
- 722 McGuire, P., A. Spence, F. Stalkup, M. Cooley, et al. (1995), Core acquisition and analy-
723 sis for optimization of the prudhoe bay miscible-gas project, *SPE reservoir engineering*,
724 10(02), 94–100.
- 725 Michael, K., A. Golab, V. Shulakova, J. Ennis-King, G. Allinson, S. Sharma, and T. Aiken
726 (2010), Geological storage of co₂ in saline aquifers—a review of the experience from ex-
727 isting storage operations, *International journal of greenhouse gas control*, 4(4), 659–667.
- 728 Mori, H., T. Sakaki, and T. H. Illangasekare (2015), Laboratory study of geological carbon
729 sequestration using surrogate fluids: Dielectric measurement and scaling of capillary
730 pressure-saturation relationships, *International Journal of Greenhouse Gas Control*, doi:
731 10.1016/j.ijggc.2015.01.023.
- 732 Mouche, E., M. Hayek, and C. Mügler (2010), Upscaling of CO₂ vertical migration through
733 a periodic layered porous medium: The capillary-free and capillary-dominant cases, *Ad-
734 vances in Water Resources*, doi:10.1016/j.advwatres.2010.07.005.

- 735 Neumann, R., P. Bastian, and O. Ippisch (2013), Modeling and simulation of two-phase two-
736 component flow with disappearing nonwetting phase, *Computational Geosciences*, 17(1),
737 139–149, doi:10.1007/s10596-012-9321-3.
- 738 Nordbotten, J. M., and M. A. Celia (2006), Similarity solutions for fluid injection into con-
739 fined aquifers, *Journal of Fluid Mechanics*, doi:10.1017/S0022112006000802.
- 740 Obi, E.-O. I., and M. J. Blunt (2006), Streamline-based simulation of carbon dioxide storage
741 in a north sea aquifer, *Water Resources Research*, 42(3).
- 742 Oh, J., K. Y. Kim, W. S. Han, E. Park, and J. C. Kim (2015), Migration behavior of supercrit-
743 ical and liquid CO₂ in a stratified system: Experiments and numerical simulations, *Water*
744 *Resources Research*, doi:10.1002/2015WR017022.
- 745 Oldenburg, C. M., and A. P. Rinaldi (2011), Buoyancy Effects on Upward Brine Dis-
746 placement Caused by CO₂ Injection, *Transport in Porous Media*, doi:10.1007/
747 s11242-010-9699-0.
- 748 Onoja, M. U., J. D. Williams, H. Vosper, and S. M. Shariatipour (2019), Effect of sedimen-
749 tary heterogeneities in the sealing formation on predictive analysis of geological co₂ stor-
750 age, *International Journal of Greenhouse Gas Control*, 82, 229–243.
- 751 Plampin, M. R., R. N. Lassen, T. Sakaki, M. L. Porter, R. J. Pawar, K. H. Jensen, and T. H.
752 Illangasekare (2014), Heterogeneity-enhanced gas phase formation in shallow aquifers
753 during leakage of CO₂-saturated water from geologic sequestration sites, *Water Resources*
754 *Research*, doi:10.1002/2014WR015715.
- 755 Plug, W. J., and J. Bruining (2007), Capillary pressure for the sand-CO₂-water system under
756 various pressure conditions. Application to CO₂ sequestration, *Advances in Water Re-*
757 *sources*, doi:10.1016/j.advwatres.2007.05.010.
- 758 Pruess, K., and J. Nordbotten (2011), Numerical Simulation Studies of the Long-term Evo-
759 lution of a CO₂ Plume in a Saline Aquifer with a Sloping Caprock, *Transport in Porous*
760 *Media*, doi:10.1007/s11242-011-9729-6.
- 761 Rasmusson, K., C.-F. Tsang, Y. Tsang, M. Rasmusson, L. Pan, F. Fagerlund, J. Bensabat, and
762 A. Niemi (2015), Distribution of injected co₂ in a stratified saline reservoir accounting for
763 coupled wellbore-reservoir flow, *Greenhouse Gases: Science and Technology*, 5(4), 419–
764 436.
- 765 Redlich, O., and J. N. Kwong (1949), On the thermodynamics of solutions. V. An equation of
766 state. Fugacities of gaseous solutions, *Chemical Reviews*, doi:10.1021/cr60137a013.
- 767 Renard, P., and G. de Marsily (1997), Calculating equivalent permeability: a review, *Ad-*
768 *vances in Water Resources*, 20(5), 253–278, doi:https://doi.org/10.1016/S0309-1708(96)
769 00050-4.
- 770 Riaz, A., M. HESSE, H. A. TCHELEPI, and F. M. ORR (2006), Onset of convection in a
771 gravitationally unstable diffusive boundary layer in porous media, *Journal of Fluid Me-*
772 *chanics*, 548, 87–111, doi:10.1017/S0022112005007494.
- 773 Saaltink, M. W., V. Vilarrasa, F. De Gaspari, O. Silva, J. Carrera, and T. S. Rötting (2013),
774 A method for incorporating equilibrium chemical reactions into multiphase flow models
775 for co₂ storage, *Advances in Water Resources*, 62, 431 – 441, doi:https://doi.org/10.1016/j.
776 advwatres.2013.09.013, computational Methods in Geologic CO₂ Sequestration.
- 777 Sanchez-Vila, X., A. Guadagnini, and J. Carrera (2006), Representative hydraulic conductiv-
778 ities in saturated groundwater flow, *Reviews of Geophysics*, 44(3), doi:https://doi.org/10.
779 1029/2005RG000169.
- 780 Schwartz, M. O. (2014), Modelling leakage and groundwater pollution in a hypothetical co₂
781 sequestration project, *International Journal of Greenhouse Gas Control*, 23, 72–85.
- 782 Silin, D., T. Patzek, and S. M. Benson (2009), A model of buoyancy-driven two-phase coun-
783 tercurrent fluid flow, *Transport in Porous Media*, 76(3), 449–469.
- 784 Spycher, N., and K. Pruess (2005), CO₂-H₂O mixtures in the geological sequestration of
785 CO₂. II. Partitioning in chloride brines at 12–100°C and up to 600 bar, *Geochimica et Cos-*
786 *mochimica Acta*, doi:10.1016/j.gca.2005.01.015.
- 787 Spycher, N., K. Pruess, and J. Ennis-King (2003), CO₂-H₂O mixtures in the geological se-
788 questration of CO₂. I. Assessment and calculation of mutual solubilities from 12 to 100°C

- 789 and up to 600 bar, *Geochimica et Cosmochimica Acta*, doi:10.1016/S0016-7037(03)
790 00273-4.
- 791 Stalkup, F., and S. Crane (1994), Reservoir description detail required to predict solvent and
792 water saturations at an observation well, *SPE Reservoir Engineering*, 9(01), 35–43.
- 793 Strandli, C. W., and S. M. Benson (2013), Identifying diagnostics for reservoir structure and
794 CO₂ plume migration from multilevel pressure measurements, *Water Resources Research*,
795 doi:10.1002/wrcr.20285.
- 796 Sung, R.-T., M.-H. Li, J.-J. Dong, A. T.-S. Lin, S.-K. Hsu, C.-Y. Wang, and C.-N. Yang
797 (2014), Numerical assessment of CO₂ geological sequestration in sloping and layered het-
798 erogeneous formations: A case study from taiwan, *International Journal of Greenhouse
799 Gas Control*, 20, 168–179.
- 800 Szulczewski, M. L., C. W. MacMinn, H. J. Herzog, and R. Juanes (2012), Lifetime of car-
801 bon capture and storage as a climate-change mitigation technology, *Proceedings of the
802 National Academy of Sciences*, 109(14), 5185–5189.
- 803 Trevisan, L., A. Cihan, F. Fagerlund, E. Agartan, H. Mori, J. T. Birkholzer, Q. Zhou, and
804 T. H. Illangasekare (2014), Investigation of mechanisms of supercritical CO₂ trapping in
805 deep saline reservoirs using surrogate fluids at ambient laboratory conditions, *Internat-
806 ional Journal of Greenhouse Gas Control*, doi:10.1016/j.ijggc.2014.07.012.
- 807 Trevisan, L., R. Pini, A. Cihan, J. T. Birkholzer, Q. Zhou, and T. H. Illangasekare (2015),
808 Experimental analysis of spatial correlation effects on capillary trapping of supercritical
809 CO₂ at the intermediate laboratory scale in heterogeneous porous media, *Water Resources
810 Research*, doi:10.1002/2015WR017440.
- 811 Tsang, C.-F., Y. W. Tsang, J. Birkholzer, and L. Moreno (2001), Dynamic channeling of
812 flow and transport in saturated and unsaturated heterogeneous media, *GEOPHYSICAL
813 MONOGRAPH-AMERICAN GEOPHYSICAL UNION*, 42, 33–44.
- 814 Van der Meer, L. (1995), The CO₂ storage efficiency of aquifers, *Energy conversion and man-
815 agement*, 36(6-9), 513–518.
- 816 van Genuchten, M. T. (1980), A Closed-form Equation for Predicting the Hydraulic Con-
817 ductivity of Unsaturated Soils1, *Soil Science Society of America Journal*, doi:10.2136/
818 sssaj1980.03615995004400050002x.
- 819 Vilarrasa, V., D. Bolster, M. Dentz, S. Olivella, and J. Carrera (2010), Effects of CO₂ Com-
820 pressibility on CO₂ Storage in Deep Saline Aquifers, *Transport in Porous Media*, doi:
821 10.1007/s11242-010-9582-z.
- 822 Wang, K., T. Xu, H. Tian, and F. Wang (2016), Impacts of mineralogical compositions on
823 different trapping mechanisms during long-term CO₂ storage in deep saline aquifers, *Acta
824 Geotechnica*, 11(5), 1167–1188.
- 825 Wang, Y. (2022), Numerical modeling of geological carbon sequestration: Enhanced dissolu-
826 tion in randomly heterogeneous media, Ph.D. thesis, Technical University of Catalonia.
- 827 Wen, X.-H., and J. Gómez-Hernández (1996), Upscaling hydraulic conductivities in het-
828 erogeneous media: An overview, *Journal of Hydrology*, 183(1), ix–xxxii, doi:https:
829 //doi.org/10.1016/S0022-1694(96)80030-8.
- 830 Xiao, T., B. McPherson, R. Esser, W. Jia, N. Moodie, S. Chu, and S.-Y. Lee (2019), Fore-
831 casting commercial-scale CO₂ storage capacity in deep saline reservoirs: Case study of
832 Buzzard’s bench, central Utah, *Computers & Geosciences*, 126, 41–51.
- 833 Xu, T., E. Sonnenthal, N. Spycher, and K. Pruess (2004), Toughreact user’s guide: A simu-
834 lation program for non-isothermal multiphase reactive geochemical transport in variable
835 saturated geologic media, *Tech. rep.*, Lawrence Berkeley National Lab.(LBNL), Berkeley,
836 CA (United States).
- 837 Xu, T., N. Spycher, E. Sonnenthal, G. Zhang, L. Zheng, and K. Pruess (2011), Toughreact
838 version 2.0: A simulator for subsurface reactive transport under non-isothermal multi-
839 phase flow conditions, *Computers & Geosciences*, 37(6), 763–774.
- 840 Zhang, M., Y. Zhang, and P. Lichtner (2017), Evaluating model complexity in simulating su-
841 percritical CO₂ dissolution, leakage, footprint, and reservoir pressure for three-dimensional
842 hierarchical aquifer, *International Journal of Greenhouse Gas Control*, 64, 284–299.

- 843 Zhao, B., C. W. MacMinn, and R. Juanes (2014), Residual trapping, solubility trapping and
844 capillary pinning complement each other to limit co₂ migration in deep saline aquifers,
845 *Energy Procedia*, 63, 3833–3839.
- 846 Zhou, Q., J. T. Birkholzer, C.-F. Tsang, and J. Rutqvist (2008), A method for quick assess-
847 ment of co₂ storage capacity in closed and semi-closed saline formations, *International*
848 *Journal of Greenhouse gas control*, 2(4), 626–639.
- 849 Zhou, Q., J. T. Birkholzer, E. Mehnert, Y.-F. Lin, and K. Zhang (2010), Modeling basin-and
850 plume-scale processes of co₂ storage for full-scale deployment, *Groundwater*, 48(4), 494–
851 514.
- 852 Zinn, B., and C. F. Harvey (2003), When good statistical models of aquifer heterogeneity go
853 bad: A comparison of flow, dispersion, and mass transfer in connected and multivariate
854 gaussian hydraulic conductivity fields, *Water Resources Research*, 39(3), doi:10.1029/
855 2001WR001146.